6-15-2008

# Bandstructure Effects in Silicon Nanowire Electron Transport

Neophytos Neophytou
*Purdue University - Main Campus*

Abhijeet Paul
*Purdue University - Main Campus*

Mark S. Lundstrom
*Purdue University - Main Campus*

Gerhard Klimeck
*Purdue University - Main Campus*, gekco@purdue.edu

# Bandstructure Effects in Silicon Nanowire Electron Transport

Neophytos Neophytou, Abhijeet Paul, Mark S. Lundstrom, and Gerhard Klimeck

***Abstract*—Bandstructure effects in the electronic transport of strongly quantized silicon nanowire field-effect-transistors (FET) in various transport orientations are examined. A 10-band $sp^3d^5s^*$ semiempirical atomistic tight-binding model coupled to a self-consistent Poisson solver is used for the dispersion calculation. A semi-classical, ballistic FET model is used to evaluate the current-voltage characteristics. It is found that the total gate capacitance is degraded from the oxide capacitance value by 30% for wires in all the considered transport orientations ([100], [110], [111]). Different wire directions primarily influence the carrier velocities, which mainly determine the relative performance differences, while the total charge difference is weakly affected. The velocities depend on the effective mass and degeneracy of the dispersions. The [110] and secondly the [100] oriented 3 nm thick nanowires examined, indicate the best ON-current performance compared to [111] wires. The dispersion features are strong functions of quantization. Effects such as valley splitting can lift the degeneracies particularly for wires with cross section sides below 3 nm. The effective masses also change significantly with quantization, and change differently for different transport orientations. For the cases of [100] and [111] wires the masses increase with quantization, however, in the [110] case, the mass decreases. The mass variations can be explained from the non-parabolicities and anisotropies that reside in the first Brillouin zone of silicon.**

***Index Terms*—Anisotropy, bandstructure, effective mass, injection velocity, MOSFETs, nanowire, nonparabolicity, quantum capacitance, tight binding, transistors.**

## I. Introduction

As TRANSISTOR sizes shrink down to the nanoscale, CMOS development investigates alternative structures and devices [1]. Existing CMOS field effect transistors are expected to evolve from planar to 3-D nonplanar devices at nanometer sizes. A possible device approach that has attracted much attention recently because of its possibility of enhanced electrostatic control, is the use of nanowire (NW) transistors as field effect devices. Nanowire transistors of diameters even down to 3 nm have already been demonstrated by various experimental groups [2]–[4]. Under extreme scaling of the device's dimensions, the atoms in the cross section will be countable, and crystal symmetry, bond orientation, and quantum mechanical confinement will matter. Proper atomistic modeling is therefore essential in understanding the electrical characteristics of ultra-scaled cross section nanowire devices. This work identifies the main bandstructure parameters that influence the transport properties of nanowire devices by using a nearest-neighbor tight binding (TB) model ($sp^3d^5s^*$) [5]–[8] for electronic structure calculation, coupled to a 2-D Poisson solver for electrostatics. A simple semiclassical ballistic model [9], [10] [Fig. 1(a)] is used to evaluate transport characteristics. The ballistic transport characteristics of square nanowires 3 nm wide, oriented in [100], [110], and [111] transport directions were examined and compared.

The electrostatic potential variations in the lattice were calculated using a 2-D Poisson solver. Self-consistently accounting

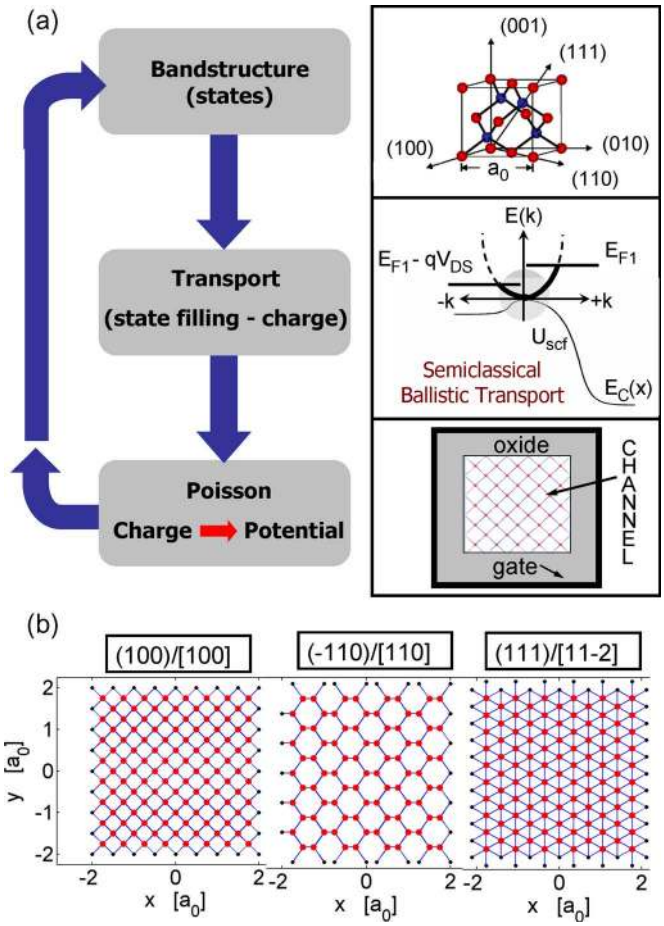


Fig. 1. (a) Schematic of the simulation procedure. Using an atomistic $sp^3d^5s^*$ tight-binding model, the bandstructure of the nanowire under consideration is calculated. A semiclassical ballistic model is then used to calculate the charge distribution in the wire from the source and drain Fermi levels. The charge is used in a 2-D Poisson solver for the electrostatic solution of the potential in the cross section of the wire. The whole process is performed self-consistently. (b) The lattice in the wire transport orientations (surfaces) used. [100], [110], and [111] orientations.

Manuscript received October 5, 2007; revised February 20, 2008. This work was funded by the Semiconductor Research Corporation (SRC) and MARCO MSD Focus Center on Materials, Structures and Devices. The review of this paper was arranged by Editor M. Reed.

The authors are with the School of Electrical and Computer Engineering, Purdue University, West Lafayette, IN 47907-1285 USA (e-mail: neophyto@purdue.edu).

Color versions of one or more of the figures in this paper are available online at http://ieeexplore.ieee.org.

Digital Object Identifier 10.1109/TED.2008.920233

for the potential variations in the nanowire cross section is a critical step in evaluating nanowire transport characteristics. Although this factor causes only small shifts of energy levels, and weak lifting of degeneracies, it strongly influences the charge placement in the cross section of the wire. The charge placement, together with the small 1-D density of states in nanowires, strongly degrades the capacitance of the device by up to 30% and affects its performance. This degradation is the same for all wire orientations. We show that the carrier injection velocities (controlled by the transport mass) and the degeneracies (controlled by orientation) are the dominant determining factors of the relative device performance for different wire orientations. In terms of ON-current capabilities, transport at small nanowire dimensions will be preferable in the [110]-oriented devices that have the lowest mass and highest carrier velocities, closely followed by the [100] devices with somewhat higher masses. The [111] nanowires indicate a lower performance due to their much heavier transport masses, in agreement with [11]. As also shown by other authors, the masses and degeneracies are strong functions of not only directionality, but also of structural quantization [12]–[14]. Specifically, for the case of mass variations, this paper shows how quantization affects the masses differently in different transport orientations. It is a result of the nonparabolicity and anisotropy of the Si bandstructure that is particularly evident in strongly quantized nanowires. Wires in [110] transport orientation experience a reduction in the electron transport effective mass compared to [100]- or [111]-oriented wires. A simple analytical approach, presented in this paper, provides insight in understanding these variations. Other effects, such as valley splitting, also have directional dependence and are significantly enhanced in [110] nanowires compared to [100] or [111] nanowires.

*Necessity of Atomistic Modeling:* The effects investigated in this study are mainly atomistic effects, which the usual effective mass approximation (EMA) fails to capture. When we compare devices in different orientations, the devices' atomistic descriptions have the advantage of being able to capture the valley projections automatically and extract the dispersions of the nanowires in the transport orientation. Atomistic modeling also automatically includes information about band coupling and mass variations as functions of quantization. The problem of identifying the correct bandstructure and effective masses of nanowires has been addressed by various authors [15]–[18] with qualitative agreement on the main features of the electronic structures. Other sophisticated techniques for electronic structure calculation also mention mass variations in nanostructures from their bulk values, which results in different threshold voltages and ON-current densities [15], [19]. The EMA can still be used [15], [20] for the conduction band only when we adjust the effective masses to map masses extracted from atomistic calculations, particularly for [100] oriented nanowires, and in some cases for other orientations. In general, however, this method is not always valid, and atomistic simulations are more appropriate for nanowires of a few nanometers cross-sectional sides.

This paper is organized as follows. In Section II, the TB model, its validity, and the simulation approach is described. Section III contains the numerical results. Section III-A examines the behavior of bandstructure under charge filling of the lattice for nanowires in different orientations for 3 nm cross-sectional side square nanowires. Section III-B compares the performance of nanowires of different orientations in terms of total gate capacitance, quantum capacitance, injection velocity, and drive current capabilities. Explanations for the relative performance are given in terms of the most important dispersion properties (masses and degeneracies). Section III-C examines how structural quantization will impact the dispersions of wires with different cross sectional areas. Valley splitting and the mass variation in wires of different cross sections are examined. Finally, in Section III-D an explanation of the dispersion mass and band-edge variation is given using extracted bands from the bulk bandstructure. Section IV summarizes and concludes the paper.

## II. Approach

*Motivation for an Empirical TB Model:* At the nanometer scale, the concept of "new device" and "new material" are blurred. Quantum mechanics of the electronic structure, crystal symmetry, atomic composition, and spatial disorder are important. A certain electronic structure model needs to satisfy several requirements to capture nanoscale device physics accurately. The finite extent of the devices, rather than the infinite periodic nature, speaks for the choice of a local basis set rather than a planewave basis set. The stability of the bands in typical semiconductor devices speaks for a reduced model that takes the existence of bands for granted. The need to model complicated man-made heterostructures speaks for a nearest neighbor model to eliminate ambiguities of long-range coupling elements. The need to simulate large extensive structures containing tenths of millions of atoms [7] requires a reduced-order model. The need to accurately model bandgaps (within a few millielectron volts) and masses (within a few percent) speaks for an empirical bandstructure model, rather than an ab initio model. All these requirements have led to the choice of empirical tight-binding (TB) in this work.

*The $sp^3d^5s^*$ TB Model:* The basis set of the $sp^3d^5s^*$ nearest neighbor TB model used in this work is composed of orthogonal localized orbitals. This type of basis makes it very attractive for accurate electronic structure of truncated nanostructures of finite sizes and composition variations on a nanometer scale. It is a very convenient method for treating material and potential variations as well as strain fields. Parameterization was performed using a genetic algorithm in [5], and the parameters extracted can reproduce the band edges of the bulk silicon bandstructure over the entire Brillouin zone. The model is described in detail in [5]–[8]. The energy bands obtained for nanowires, as well as for the bulk case in energy regions away from the bulk minima, are in good quantitative agreement with other theoretical calculations using pseudopotential and ab initio GW methods.[1] In this work, the electrostatic potential for charge self-consistency is also included on the ON-sides of the

[1]Personal communication with Prof. Mark Schilfgaarde (Arizona State University) for the GW calculations and with Dr. Tony Low (Purdue University) for the pseudopotential calculations. A comparison between the methods will be published in the future.

Hamiltonian matrix in an effective potential approach, which shifts the bands with no further change in connectivity.

*Validation of the Model Through Experimental Data:* Because the accuracy of the results presented here strongly depends on the validity of the TB model used, particularly on its transferability to nanostructures, it is convincing to mention that the same model and calibration parameters were used to explain experimental data in a variety of applications with excellent qualitative agreement. Some examples include explaining resonant tunneling diode applications for transport under high bias with charge self-consistency [21]–[23], explaining experimental data for the bandgap of ultrascaled nanowires [24]–[26], valley splitting of tilted and disordered quantum wells [27], and the electronic structure of silicon systems with phosphorus impurities [28]. Further theoretical work presented in [29] examines the performance of core shell nanowires and validates against experimental data. Specifically, the theoretical calculation of experimental measurements of the bandgap of ultrascaled [112]-oriented nanowires in [24]–[26] is a strong validation that the model captures the essential nonparabolicities in a large part of the Brillouin zone of Si. As shown later, nonparabolicites and anisotropies at high energies strongly influence the masses and band edges of nanowires. Because the bandgap of quantized systems is a strong function of the quantization masses in the two transverse directions, verification of the experimentally deduced nanowires' bandgaps supports the theoretical prediction for the behavior of the wires' masses under strong quantization and in extent the model's validity.

*The Simulation Approach:* The simulated model device is a rectangular nanowire of $3 \times 3$ nm dimensions in various transport orientations. Unless otherwise stated, the specified wire orientation is the transport direction. Three different orientations, ([100], [110], and [111]) are investigated. The atomic arrangement in each case is different, as shown in Fig. 1(b).

The simulation procedure consists of three steps as shown in Fig. 1(a) and described below:

1) First, the bandstructure of the wire is calculated using an atomistic tight-binding model. In this case, each atomic side in the zincblende lattice is represented by a $\mathrm{sp}^3d^5\mathrm{s}^*$ basis in the wire Hamiltonian. Because only the conduction band is treated in this paper, the spin-orbit coupling is ignored. This approximation favors computational efficiency without affecting the accuracy of the results [16]. The atoms that reside on the surface of the nanowire are passivated in the $\mathrm{sp}^3$ hybridization scheme [30]. This technique successfully removes all dangling bonds that otherwise would create surface states with eigenenergies in the device's bandgap. Any effect of surface reconstruction or surface imperfections is not considered in this study. Only the channel atoms enter the atomistic calculation in the Hamiltonian construction. At this step, the energy of the dispersion states and their wavefunctions are computed. Bandstructure effects such as valley splitting and effective mass change under physical quantization are investigated at this step for the nanowire of interest, using equilibrium dispersion (flat electrostatic potential in the Hamiltonian).
2) A semiclassical top-of-the-barrier ballistic model is used to fill the dispersion states and compute the transport characteristics [9], [10]. This model assumes that the positive going states are filled according to the source Fermi level, whereas the negative going states according to the drain Fermi level. Once the occupancy of the dispersion states is computed, using their wavefunction from step 1, the charge distribution in each of the orbital sites of the system (and therefore the spatial distribution of charge) is obtained.
3) Using the charge distribution obtained in step 2, the two-dimensional (2-D) Poisson equation is solved in the cross section of the wire to obtain the electrostatic potential. The Poisson's equation is solved in 2-D, and all the atomic locations are collapsed on the 2-D plane.[2] The Poisson domain is described by a finite difference mesh and contains the nanowire core on an atomistic mesh, the dielectric, and the metal. The electrostatic potential is added to the diagonal elements of the atomistic Hamiltonian for recalculating the bandstructure until self-consistency is achieved. In this step, the oxide in all calculations is assumed to be $SiO_2$ of 1.1 nm thickness. This dielectric is not included in the Hamiltonian but is only treated in the Poisson equation as a continuum medium. Any effects due to the potential variations along the transport direction are ignored. This falls under the assumption that the carrier injection at the top of the barrier is most important to the transport properties of the device at the ballistic limit.

Although the transport model used is simplistic, it allows for examining how the bandstructure of the nanowire alone will affect its ballistic transport characteristics, ignoring any short-channel effects or quantum mechanical tunneling under the potential barrier. The same conclusion to this work can be obtained from the full 3-D quantum nonequilibrium Green's function simulations [11], but the simple model used here provides physical insight. It is also mentioned that the main conclusions of this work will be valid for other nanowire cross sections, i.e. cylindrical, since the electronic properties of nanowires are a much more sensitive function of the quantization size rather than the quantization shape [15].

## III. Results and Discussion

### A. Effect of Potential Variations on the NW Dispersion and Charge Distribution

*Description of the Dispersion in [100]-Oriented Wires:* The dispersion of a [100]-oriented nanowire is shown in Fig. 2(c). It has a four-fold degenerate valley at the $\Gamma$ point ($k_x = 0$) resulting from the $k$-space projection of the four silicon ellipsoids that reside in the plane of quantization (here, the $y-z$ plane). There are two more valleys residing off-$\Gamma$ (one in the positive and one in the negative $k_x$ axis), that result from the

[2]We have conducted extensive tests to validate the 2-D Poisson solution compared to the actual 3-D solution. A maximum deviation of 2% on the band edges between the two approaches was found, as well as ignorable deviation in the I-V characteristics. However, the 2-D method reduces the Poisson computational time by almost $5\times$ compared to the 3-D solution.

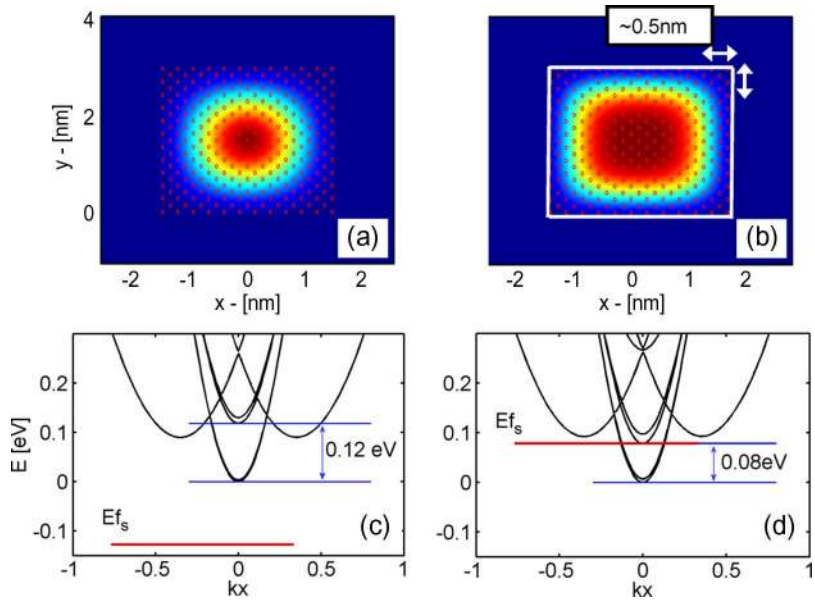


Fig. 2. The 3-nm [100] rectangular wire. (a), (b) Two-dimensional cross section showing the charge distribution under low and high gate biases, respectively. Even under high bias, the charge distribution is located almost half a nanometer away from the oxide. This causes degradation in the total capacitance of the wire. The dots indicate the underlying atomic positions. (c), (d) $E(k)$ plots for (a) and (b). The bandstructure features change under self-consistency. $E_{fs}$ is the source Fermi level. (Zero energy indicates the conduction subband edge.)

two off-plane ellipsoids. The first four appear lower in energy because of their heavy quantization mass ($m_y \sim m_l = 0.89$ m$_0$ and $m_z \sim m_t = 0.19$ m$_0$) and have lighter transport mass ($m_x \sim m_t = 0.19$ m$_0$). The other two appear at higher energies because of the lighter quantization masses ($m_y \sim m_t = 0.19$ m$_0$ and $m_z \sim m_t = 0.19$ m$_0$) and have heavier transport mass ($m_x \sim m_t = 0.89$ m$_0$). (The wire masses $m_x$, $m_y$, $m_z$ are close, but not exactly the bulk longitudinal and transverse masses for reasons that will be addressed later on).

*Change of the [100] Wire Dispersion Due to Potential Variations/Charge Filling:* The first part of this section investigates how potential variations in the cross section of a wire can change the dispersion and how the wavefunction shape changes as the lattice fills up with a charge. Fig. 2 shows device features for a 3 × 3 nm [100]-oriented nanowire under low and high gate biases. (The drain bias used is $V_D = 0.5$ V in all cases throughout this work.) Under low gate biases, the lattice is almost empty of charge [Fig. 2(a)], and the dispersion relation [Fig. 2(c)] is the equilibrium dispersion. Under high biases, there is significant charge filling of the lattice, as shown in Fig. 2(b). The charge distribution takes the shape of the underlying atomic positions. In these simulations, even under high-inversion conditions, the wavefunction is pushed almost 0.5 nm away from the Si/SiO$_2$ interface. The dispersion of these small-sized nanowires, on the other hand, is usually considered to be a material parameter and a property of the geometry under strong confinement but independent of charge filling of the lattice. Fig. 2(d) shows, however, that charge filling of the lattice causes changes in the dispersion of the nanowire, even at the 3-nm wire length scale. Here, the excited states at $\Gamma$ shift down and now reside below the off-$\Gamma$ point valleys. In this case, the change in the dispersion is small, but because it is associated with the wavefunction shape that gives rise to the charge distribution in the wire cross section, it can affect the device's capacitance and, to some extent, its transport characteristics.

*Change of the [110] Wire Dispersion Due to Potential Variations/Charge Filling:* The change in the dispersion under potential variations is also observed in different wire orientations, which have different dispersion relations. The position of the bands shifts and degeneracies can also be lifted. Fig. 3(a) and (b) shows the $E(k)$ of a [110]-oriented nanowire under low and high biases. The dispersion looks different from the [100] dispersion, with a two-fold degenerate band at $\Gamma$ and a pair of two-fold degenerate bands off-$\Gamma$. A larger variation in the dispersion under charge filling of the lattice is observed compared to the [100] wire case. The band degeneracies are lifted (from 2 to 1) by several millielectron volts. This is an effect that cannot be captured in a simple EMA treatment.

*Change of the [111] Wire Dispersion Due to Potential Variations/Charge Filling:* Fig. 3(c) and (d) shows the same features for a [111]-oriented wire. The degeneracy of the bands of this wire is 3 (for each valley) because of the symmetry between the transport axis (or, equivalently, the quantization plane in the perpendicular direction) and the three pairs of ellipsoids in the Si bandstructure. High biases increase band coupling, which slightly lifts the degeneracies. Note that in the case of [100] and [110] wires, the conduction band minima is located at the $\Gamma$ point because the quantized $\Delta$ valleys project there. In the [111] case, however, the conduction band minimum is located at 0.37 of the Brillouin zone (normalized to 1) as seen in Fig. 3(c) and (d).[3]

[3]The length of the unit cell in [111] is $L_{111} = \sqrt{3}a_0$. Therefore, the Brillouin zone of a 1-D nanowire in [111] extends from $-\pi/\sqrt{3}a_0$ to $\pi/\sqrt{3}a_0$. The $\Delta$ valleys in bulk Si are located at $k_x = 0.815 \cdot 2\pi/a_0$. Under quantization in a (111) surface the valleys project on the [111] axis at $k_{[111]} = 0.815 \cdot 2\pi/(\sqrt{3}a_0) = 1.63\pi/(\sqrt{3}a_0)$. The valley projection point falls in the second Brillouin zone. It is then folded in the first Brillouin zone as $k_{[111]} = 1.63\pi/(\sqrt{3}a_0) - 2\pi/(\sqrt{3}a_0) = 0.37\pi/(\sqrt{3}a_0)$. After normalization to the length of the Brillouin zone, the valleys appear as $k_{[111]} = 0.37$.

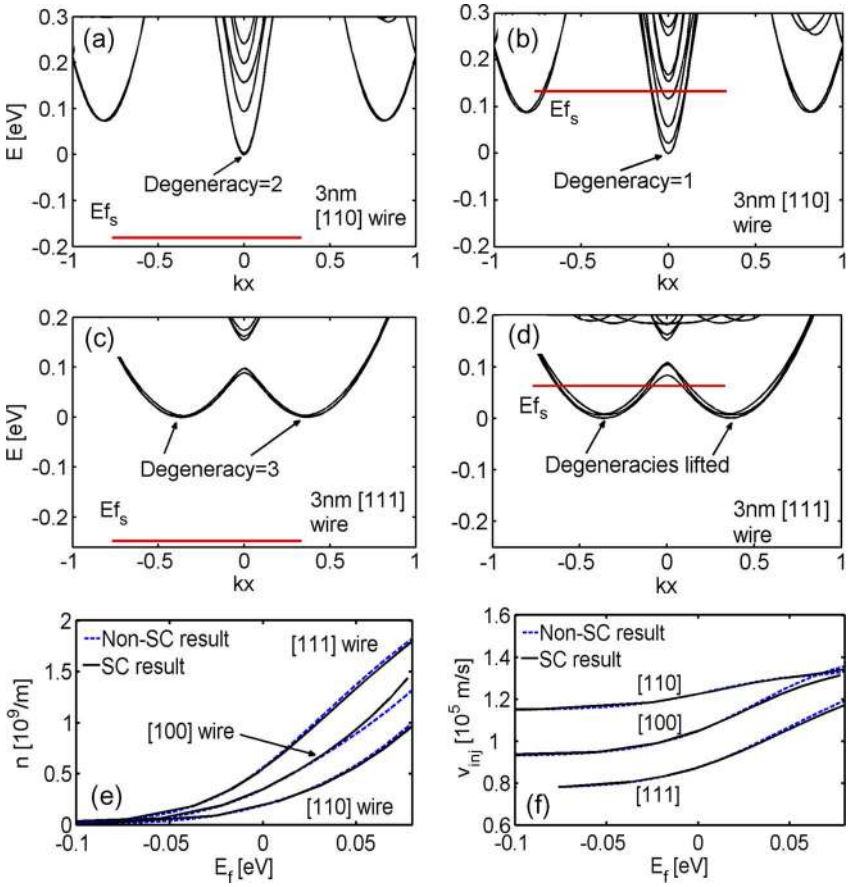


Fig. 3. (a) Bandstructure of a 3-nm [110]-oriented nanowire under low bias ($V_G = 0$ V) and (b) high bias ($V_G = 0.8$ V) and $V_D = 0.5$ V. Under high biases the degeneracies of the $\Gamma$ valley are lifted from 2 to 1. (c) Bandstructure of a 3-nm [111]-oriented nanowire under low bias ($V_G = 0$ V), (d) high bias ($V_G = 0.8$ V), and $V_D = 0.5$ V. (e) The charge in the wire as a function of the difference of the conduction band edge from the Fermi level for two cases: 1) The Fermi level "scans" the equilibrium bandstructure, and the charge is extracted. 2) The charge is extracted from the self-consistent calculations with potential variations in the lattice taken into consideration. (f) Injection velocity for the same case as (e). Changes in the dispersion themselves do not reflect much on the charge distribution or the injection velocities. The differences between the two models result from the spatial information of the wavefunction that corresponds to the bandstructure changes.

*Charge/Velocity Are Invariant to Self-Consistency:* Just by looking at these variations in the dispersion, however, it is not clear that they will result in changes in the transport characteristics. Indeed, Fig. 3(e) and (f) compares the density of states and velocities at the same $E_f - E_c$ (difference of the Fermi level from the conduction band edge) between the equilibrium dispersion and the dispersion at various biases and little difference is observed. Quantities for two cases are calculated:

1) The Fermi level "scans" the equilibrium bandstructure, and the charge and injection velocities are extracted.
2) The results are extracted from the self-consistent calculations, with potential variations in the lattice taken into consideration.

The charge and injection velocity is plotted as a function of $E_f$. ($E_c$ is shifted to zero for all wires.) There is no significant difference in these extracted quantities due to the potential variations, and the self-consistent vs. non-self-consistent curves fall almost on top of each other. In this example, a large drain bias ($V_D = 0.5$ V) is used. Under low drain biases ($V_D = 1$ meV) and low temperatures, however, where the transport energy window can be comparable or even smaller than the changes in the bandstructure, evidence of the bandstructure differences in these two quantities, as well as other quantities such as transconductance, is more likely to appear.

*Charge Distribution Is Strongly Dependent on Self-Consistency:* Although the charge and velocity appear to be only weakly modified by the self-consistent calculation, the self-consistently-extracted bandstructure corresponds to a different wavefunction shape, which reflects a different charge distribution in space. This is the quantity that causes degradation of the total gate capacitance, as will be shown later, and affects the transport characteristics, and not the dispersion changes, by themselves. Therefore, one has to also consider the change in wavefunction that is associated with the dispersion changes. (In an earlier work, [31], it is shown that the current-voltage characteristics can be significantly overestimated if the spatial variation of the charge is not considered.)

*Orientation Differences in the Charge:* The charge in Fig. 3(e) for any position of the Fermi level is always highest in the [111] wire case, due to the higher density of states and valley degeneracy. This particular wire orientation has the valleys with the heaviest mass ($0.47m_0$, where $m_0$ is the free electron mass) and the largest degeneracy ($D = 6$). Therefore, at a certain energy level ($E_f - E_c$), there are more states

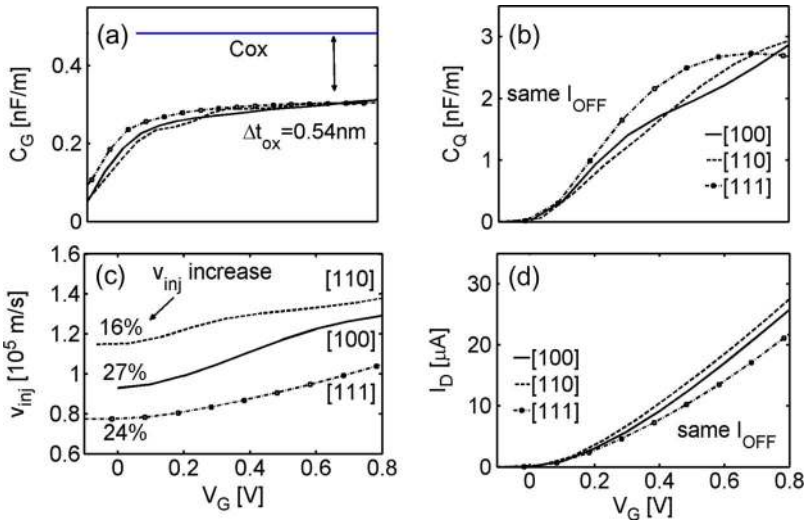


Fig. 4. Performance comparison of the 3-nm square wires in the [100], [110], and [111] directions at the same OFF-current ($I_{\rm OFF}$). (a) Gate capacitance $C_G$ vs. gate bias ($V_G$). The capacitance is similar for all wires and is degraded from the oxide capacitance by an amount that corresponds to an increase in the effective oxide thickness of 0.54 nm. (b) Quantum capacitance $C_Q$ vs. $V_G$ of the three devices, which is a measure of the density of states at the Fermi level. (c) Comparison between the injection velocities of the nanowires vs. $V_G$. In all cases, the velocity is not constant but increases as the gate bias increases. The increase is calculated by the difference between the value at high $V_G$ and the value at low $V_G$. (d) $I_{\rm DS}$ vs. $V_G$ for the three wires at the same $I_{\rm OFF}$. The velocity difference directly reflects on the current differences.

occupied compared to the other wires. The [100] wire of mass $0.27m_0$ and $D = 4$ of the lowest valley, follows. The [110] wire has the lowest charge density at a certain energy level because of its lighter mass ($0.16m_0$) and lower degeneracy ($D = 2$) at $\Gamma$.

*Orientation Differences in the Velocity:* The reverse trend is observed in Fig. 3(f), where the [110] wire has the highest velocity due to its lighter mass ($0.16m_0$). Because the higher $k$ states are occupied, the velocity increases since it is proportional to the slope of the bands. Noticeable here is the fact that the carrier velocity in the [100] wire approaches [110] velocity as the Fermi level is pushed into the conduction band. The lighter masses ($0.16m_0$) of the two-fold $\Gamma$ valleys in the [110] wire give an initial advantage over the heavier ($0.27m_0$) [100] wire $\Gamma$ valley masses. Once the heavier four-fold degenerate off-$\Gamma$ valleys (with mass $0.61m_0$) of the [110], and the heavy two-fold degenerate off-$\Gamma$ valleys (with mass $0.94m_0$) of the [100] start to populate, the carrier velocities become comparable in the two cases. The exact reasons why the masses have these values will be addressed later in the paper; however, this analysis can guide us through the reasons why wires in different transport orientations have different properties.

### *B. Device Performance Comparison of NWS in Different Orientations*

One of the points made in the previous paragraph is the comparison of the different wire orientations at the same Fermi level position into the dispersion of the wires. Although this is a rough estimate of the wires' properties, the Fermi level is not at the same position for all devices, except under special cases. In this section, the full self-consistent model is implemented to compare the performance of the nanowires. Fig. 4 shows a performance comparison between the wires in the [100], [110], and [111] orientations. The various performance quantities shown further on are all compared at the same OFF current ($I_{\rm OFF}$) for all devices.

*Gating Induces Same Capacitance/Charge in All Wire Directions:* Fig. 4(a) shows the total gate capacitance ($C_G$) vs. gate bias ($V_G$) of the three wires at the same $I_{OFF}$. The total capacitance in the three wires is very similar for all gate biases for reasons we will explain later. However, this is an indication that the same amount of inversion charge is accumulated in all wires regardless of their orientations. Our calculation supports this argument too, showing that the charge difference between the wires at high inversion does not exceed 2%. In a relative performance comparison for wires in different orientations, therefore, the amount of charge will not affect the relative performance.

*Low Semiconductor Capacitance ($C_S$) Degrades the Gate Capacitance ($C_G$) by 30%:* It is important to notice that the capacitance value is degraded from the oxide capacitance by almost 30% for all three wire cases. This is an amount that corresponds to an effective increase in the oxide thickness of 0.54 nm, which is 50% of the physical gate oxide thickness ($t_{\rm OX} = 1.1$ nm). This large gate control reduction is evidence of the low semiconductor capacitance ($C_S$) in low-dimensional channels. The gate capacitance of a device is the series combination of the oxide capacitance ($C_{\rm OX}$) and the semiconductor capacitance ($C_S$) given by the simple relation $C_G = C_S C_{OX}/(C_S + C_{OX})$. For an electrostatically well-behaved MOSFET device, $C_S$ should be an order of magnitude larger than $C_{\rm OX}$ so that the $C_G$, and therefore the charge in the device, is totally controlled by the gate. In this example, the oxide capacitance of the rectangular structure is 0.483 nF/m, numerically calculated using a 2-D Poisson solver that takes the fringing at the edges into consideration. With $C_G = 0.3$ nF/m [maximum value of Fig. 4(a)], $C_S$ can be computed to be $C_S = 0.8$ nF/m, which is only twice the value of the oxide capacitance (less than an order of magnitude difference).

*$C_S$ Controlling Factors: Charge Distribution Peak, Small $C_Q$:* $C_S$ is defined as the differential of the charge in the device with respect to the surface potential $(\psi_S)$. In 1-D systems, under a single-band effective mass approximation, the charge is the integral of the 1-D density of states $(g_{1-D})$ convoluted with the Fermi function $(f(E_f - E))$ over energy as

$$C_S = \frac{\partial(qn_s)}{\partial\psi_s} = \frac{\partial}{\partial\psi_s}\left(\int qg_{1D} f\left[(E_f - E_c - \varepsilon_i)/k_BT\right] dE\right) \tag{1a}$$

where $q$ is the charge of the electron, $\psi_s$ is the surface potential, $E_f$ is the Fermi level, $E_c$ is the conduction band edge, and $\varepsilon_i$ is the distance of the $i$th quantized subband above $E_c$ in energy. Carrying on the integration, the equation above results in

$$C_S = \frac{q^2}{\pi}\left(\frac{2m}{\hbar^2}\right)^{1/2}\sqrt{k_BT}\sqrt{\pi} \times \frac{\partial}{\partial q\psi_s}\left(\Im_{-1/2}\left[(E_f - E_c - \varepsilon_i)/k_BT\right]\right) \tag{1b}$$

$$= q^2\left(\frac{2m}{\pi\hbar^2}\right)^{1/2}\sqrt{k_BT} \times \Im_{-3/2}\left[(E_f - E_c - \varepsilon_i)/k_BT\right]\left(1 - \frac{\partial\varepsilon_i}{\partial\psi_s}\right) \tag{1c}$$

$$= C_Q\left(1 - \frac{\partial\varepsilon_i}{\partial\psi_s}\right). \tag{1d}$$

The first part of (1c), $C_Q$, is the quantum capacitance, which is a measure of the density of states at the Fermi level. $C_S$ is degraded from $C_Q$ by a factor that is proportional to how much $\varepsilon_i$ (the difference of the $i$th subband to $E_c$) changes. Ideally, at high inversion conditions, $\varepsilon_i$ should be constant, meaning that the quantized levels and $E_c$ shift by same amount, and the subband levels can easily get in the potential well that forms at the $Si/SiO_2$ interface. This directly translates on the wavefunction being able to come closer to the interface as the surface is inverted more and more. However, $\varepsilon_i$ can float up as charge accumulates in the device, giving rise to the differential term in (1d), and the wavefunction stays away from the interface. As shown earlier on in Fig. 2(b), this shift is almost 0.5 nm. Other than the wavefunction shift, $C_Q$ being small is the second degrading factor of $C_S$ as indicated in (1d). Fig. 4(b) shows the $C_Q$ of the three nanowires as a function of $V_G$, calculated as the density of states at the Fermi level. Clearly, for all wires the maximum value is below 3 nF/nm, not even an order of magnitude above $C_{OX} = 0.48$ nF/nm. The fact that the position of the charge distribution degrades $C_S$ from $C_Q$ almost four times ($C_S = 0.8$ nF/m) indicates its large significance on the device's capacitance. (Similar deviations of the semiconductor capacitance from the quantum capacitance have also been observed in thin-body devices [32].)

*Variations in $C_Q$ Between Different Wire Orientations:* As shown in Fig. 4(b), in all wire cases, $C_Q$ is not constant but undergoes large transitions as the Fermi level is pushed inside the subbands at large gate biases. This is expected because $C_Q$ is a measure of the density of states at the Fermi level, and the differences in the dispersion cause differences in $C_Q$. Comparing $C_Q$ for different wire orientations, the [111] wire has the largest $C_Q$ for most of the bias range because of the higher mass $(m^* = 0.47\ m_0)$ and higher degeneracy of its valleys $(D = 6)$. The $C_Q$ drop at high biases in [111] is associated with the decreasing 1-D density of states away from the band edges and the fact that its bands flatten out at $\Gamma$ and do not extend as parabolic bands in the $k$-space, as shown in Fig. 3(d). On the other hand, the [100] and [110] wires initially have lower $C_Q$, because of their lower density of states (lighter masses and lower degeneracies). At high biases, the upper valleys of the [100] and [110] wires start to get populated, which allows a continuous increase in $C_Q$ for these wires. More specifically, because the charge in all cases is almost the same at a given bias, the same number of states in each wire needs to be occupied. The Fermi level in the [110] wire with lower mass and smaller valley degeneracies reaches the upper valleys faster (at a lower gate bias) than the [100] wire to occupy the same number of states. Once this happens, the $C_Q$ of the [110] wire surpasses the $C_Q$ of the [100] wire (around $V_G = 0.4$ V).

*Variations in $C_Q$ Do Not Cause Variations in $C_G$:* The differences in $C_Q$ are not large enough to result in differences in the total capacitances between wires in different orientations, however. As seen earlier, $C_Q$ is only partially responsible for the total capacitance degradation. The small differences in $C_Q$ are smeared out in $C_G$ by the oxide capacitance and the charge shift from the interface, which is very similar for all the above wires. (This observation can, of course, be different in the case of high-$k$ dielectric oxides in which the importance of $C_Q$ can be more pronounced.)

*Velocity Controls the Transport Differences in Different Orientated Wires:* As explained above, the charge is almost the same in all three nanowires. Because the ON-current performance is given by the product of charge times the velocity in the ballistic limit, any performance differences will result from differences in the carrier velocities if the charge is the same. Fig. 4(c) shows the injection velocities of the wires versus the gate bias $(V_G)$. The [110] wire has the largest velocities, whereas the [111] wire has the lowest. In all cases, the injection velocities are not constant but increase as the lattice is filled with a charge because faster high-energy carrier states are being populated. This increase in velocities, calculated form the initial value at low gate biases to the final value at high gate biases, can reach up to 17% in the [110] wires and even up to 27% in the [100] and 24% in the [111] wire orientation cases. When we compare the velocities of the different wires, however, the masses of the valleys determine the velocities of the carriers. (In 1-D, under the parabolic band approximation, the velocity is proportional to $v \sim 1/\sqrt{m^*}$.) As a result, the [110] wire with $m^* = 0.16\ m_0$ has the highest velocity, followed by the [100] wire with mass $m^* = 0.27\ m_0$, and finally by the [111] wire of mass $m^* = 0.47\ m_0$. The larger density of states of the [111] wire and its larger degeneracy do not allow the Fermi level to be pushed far into the conduction band. Therefore, only the lower energy and slower carries are used, and the velocity in this case is low. In the [110] wire case, the degeneracy is 2, and the subband density of states is low; therefore, the Fermi level will be pushed far into the conduction band, and faster carries will be used, as shown in Fig. 4(c).

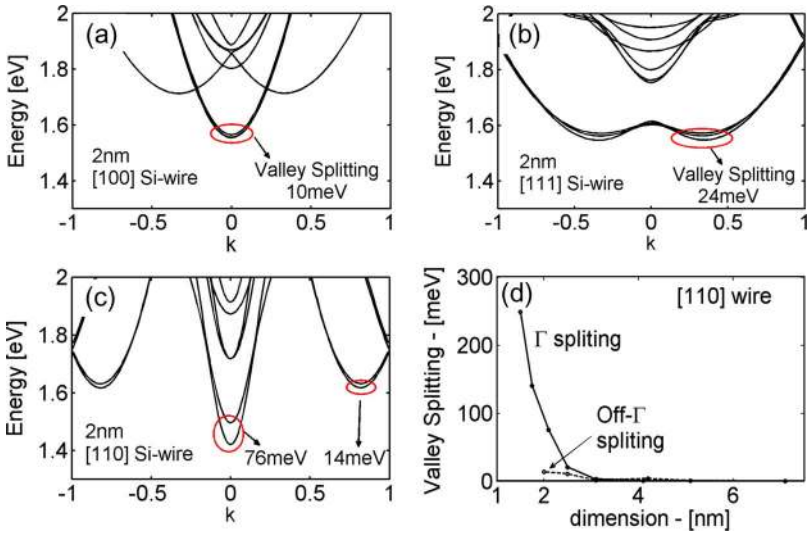


Fig. 5. Effect of valley splitting in small nanowires. (a)–(c) $E(k)$ of a 2 nm wire in the [100], [111] and [110] orientations respectively. (d) Effect of valley splitting in the [110] wire as the dimensions decrease. The Γ valleys are severely affected at cross sections below 3 nm, whereas the off-Γ valleys are not affected as much.

*Velocity Differences Affect the I–V Differences:* The velocity difference directly reflects on the $I_{\rm DS}$ as shown in Fig. 4(d), in which the drive current capabilities of the wires are compared at the same $I_{\rm OFF}$. The [110] and [100] wires perform better than the [111] wire in terms of ON-current capabilities. The current in the [110] wire stands ∼5% higher than the [100] wire and ∼20% higher than the [111] wire. This result must be qualified because the bandstructure of the wires is a very sensitive function of their quantization. The results presented here are for these specific 3-nm wire examples. In cases where important dispersion parameters such as the relative placement of the valleys in energy, masses and degeneracies are altered, different conclusions might be drawn, particularly for the relative performance of the [100] and [110] wires, which is not that large. In the next section, we analyze how exactly these parameters (valleys splittings that lift degeneracies, and masses) are affected by quantization.

### C. Quantization Influence on Valley Splitting and Mass Variation

Quantization strongly affects both factors that control the performance, the degeneracies and masses. In this section of the paper, we examine the effect of quantization on these parameters. Degeneracies are controlled mainly by the orientation but can be lifted due to valley splitting [12]–[14] under strong quantization (both electrostatic and structural).

*Weak Valley Splitting in [100] and [111] Quantized Wires:* Fig. 5(a) and (b) shows the $E(k)$ of a 2-nm wire in the [100] and [111] orientations. A slight valley splitting of the degenerate valleys under quantization is observed. In the [100], the splitting is 10 meV, and in the [111] wire the splitting is 24 meV. These values are less than the room temperature $k_BT = 26$ meV and are not expected to have a significant effect in the transport properties of the nanowires at room temperature.

*Strong Valley Splitting in [110] Quantized Wires:* In the case of [110] nanowires, valley splitting is significantly larger. As shown in Fig. 5(c) in the $E(k)$ of a 2-nm [110] wire, Γ and off-Γ valleys experience valley splitting of their degeneracies by 76 meV and 14 meV, respectively. Fig. 5(d) shows how this effect varies with the spatial confinement in the [110] wire. Although large nanowires ($>$ 5 nm) are not affected, valley splitting can reach up to 200 meV for the Γ valleys of narrow wires with sizes as narrow as 1.5 nm. The valley splitting of the off-Γ valleys, on the other hand, is not affected as much. Only a few tenths of the millielectron volts of splitting are observed in this case. (Note that the splitting in the other wire orientations is smaller than the [110] wires of similar quantization sizes, even for wires below 2 nm [14].)

*Masses Generally Increase With Increase in Quantization:* The effective mass is the second important transport performance dispersion property that is affected by quantization of the nanowire cross section. The injection velocity and quantum capacitance strongly depend on the masses. Both the quantization and the transport masses of nanowires under arbitrary wire orientations are certain combinations of the longitudinal ($m_l = 0.89$ m$_0$) and the transverse effective masses ($m_t = 0.19$ m$_0$) of the Si ellipsoids. Fig. 6(a) shows the three pairs of ellipsoids that form the conduction band minima in Si, each characterized by the $x$-, $y$-, and $z$-directional masses. The masses of the valleys that appear in the nanowire dispersion are automatically included in tight binding. What will be shown is that under quantization, the exact values of these masses are changed from their bulk values. In most cases, quantization results in an increase in the effective mass. Fig. 6(b) shows the variation in the lowest valley transport masses as the dimension of the wire cross section is reduced. At large wire cross sections, the mass of the [100] valley that is located at Γ approaches the bulk transverse mass $m_t = 0.19$ m$_0$. The bulk mass of the [111] wire is larger because it is a combination of $m_t = 0.19$ m$_0$ and $m_l = 0.89$ m$_0$ (the bulk value is $0.43m_0$) [18], [33]. The mass in the [100] case almost doubles as the dimension of the wire's side decreases from 7.1 to 1.5 nm (88% increase). (The 3-nm wire has $m^* = 0.27$ m$_0$ as mentioned earlier.) The corresponding increase in the [111] wire's mass is 17%, with

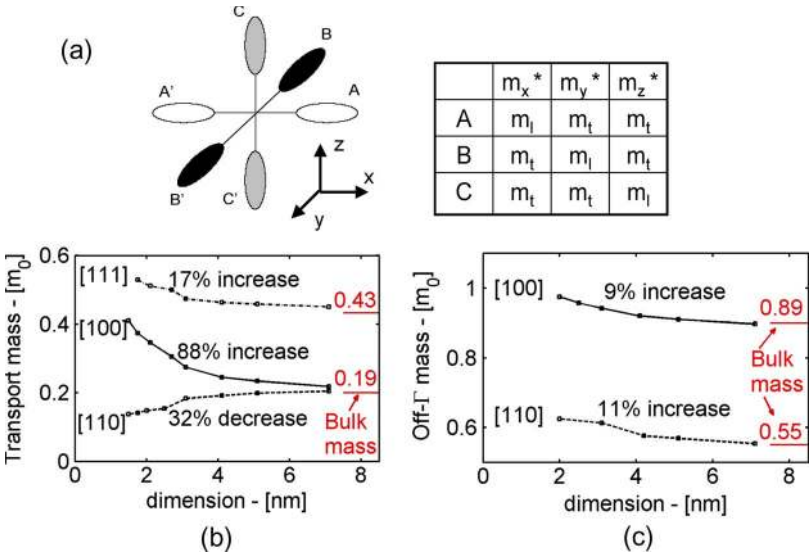


| | $m_x^*$ | $m_y^*$ | $m_z^*$ |
|---|---|---|---|
| A | $m_l$ | $m_t$ | $m_t$ |
| B | $m_t$ | $m_l$ | $m_t$ |
| C | $m_t$ | $m_t$ | $m_l$ |

Fig. 6. (a) The three equivalent pairs of ellipsoids in the conduction band of Si are described by the longitudinal and transverse masses. Combining these masses results in the quantization and transport masses of nanowires under arbitrary orientations. (b) Transport masses oriented in [100], [110], and [111] vs. the wire dimension as calculated from TB. At large wire cross sections, the [100] and [110] located at Γ approach the bulk $m_t = 0.19$ $m_0$. The mass of the [111] wire is larger because it combines $m_t$ and $m_l = 0.89$ $m_0$. As the wire dimensions shrink, the mass of the [110] wire is reduced, whereas the masses of the other two wires increase. (c) Off-Γ valley masses for the cases of the [110] and [100] wires. Both increase as the dimensions decrease. *(The bulk mass values for every orientation are denoted.)* The percentage change denoted is the change in the effective masses between the 1.5-nm mass value (mostly scaled wire) and the 7.1-nm wire.

the 3-nm wire having $m^* = 0.47$ $m_0$. The off-Γ valley masses (upper valleys) of both [100] and [110] wires also increase as the dimension reduces as shown in Fig. 6(c). In the [100] off-Γ valley case, a slight mass increase of 9% between the 7.1- and 1.5-nm wires is extracted from the bandstructure calculations. The off-Γ valley mass increase in the [110] case is 11%.

*[110] Wire Γ Valley Masses Decrease With Increase in Quantization:* In contrast to the rest of the valleys, the Γ valley mass of the [110]-oriented wires decreases with increase in quantization. As shown in Fig. 6(b) the mass decreases by 32% as the side of the wire reduces from 7.1 to 1.5 nm. As mentioned earlier, the mass of a 3-nm [110] wire is $m^* = 0.16$ $m_0$, which gives enhanced injection velocities and transport characteristics of [110] wires over the rest of the wires. Anisotropy and nonparabolicity in the Si conduction band Brillouin zone cause this unintuitive behavior, as explained in the next section.

### D. Understanding the Nanowire Mass Variation as a Function of Quantization

*Semi-Analytical Construction of the Wire's Dispersion:* This distinctly different observation in the masses of wires is a result of the nonparabolicity and anisotropy of the Si bandstructure. Under any physical quantization, the subband levels will follow the "particle in a box" quantization, seen in Fig. 7(a). The smaller the physical domain, the larger the corresponding quantized $k$, and the higher the energy levels of the subbands. To estimate the quantization levels of the Si conduction band ellipsoid quantized along the longitudinal direction, the energy contour in the $x-y$ plane near the band minima is plotted in Fig. 7(b), "cut" through the ellipsoid along its longitudinal axis. Similarly, in Fig. 7(a), quantization of $Lx$ of 2, 3, and 5 nm, respectively, will shift the energy levels to the vertical lines shown in the figure. The energy levels at these lines will be the relevant subbands in an ultrathin-body (UTB) quantization—with one quantized dimension. Fig. 7(c) now shows the energy contour taken at the 3-nm line perpendicular to the contour of Fig. 7(b) in the $y-z$ plane. An extra quantization in the $z$-direction (the second quantized dimension, as in the wire case) will leave only one allowed $k$-space variable—the transport direction one. This forms the 1-D dispersion of the wire. The relevant 1-D bands are the ones located at the horizontal lines of Fig. 7(c). Lines for $Lz = 2$, 3, and 5 nm, respectively, are shown. The solid line indicates a relative subband for an UTB device with $Lx = 3$ nm and $Lz = \infty$ ($k = 0$, only one quantization dimension).

*Mass and Band-Edge Extraction From the Semi-Analytical Construction:* The 1-D subbands of Fig. 7(c) are plotted in Fig. 7(d) for the cases of $Lz = 2$, 3, and 5 nm, respectively. (The $x$-direction quantization is $Lx = 3$ nm in all cases). The mass of these bands is the transport mass ($y$-direction) that the wire has in the [010] orientation (equivalent to the [100] wire orientation described previously). Smaller cross sections raise the subband energy and increase the masses. Through this process, we can deduce both the transport masses and the placement of the subband edges in the energy. The quantization masses can be extracted from the subband edges. The more nonparabolic the bulk bandstructure is at higher energies in the direction of quantization, the slower the subbands rise in energy with quantization, compared to the parabolic band case. This results in larger quantization masses. The more nonparabolic the bulk bandstructure is in the transport direction, the larger the transport masses will be. All these effects appear in thin-body channel devices [UTB of Fig. 6(d)], however, they are significantly more enhanced in the case of nanowires because of the extra quantization of one more physical dimension [19], [29].

*Different Orientations, Different Anisotropies:* The transport masses of wires in other orientations can be explained similarly. Evident in the bandstructure is the anisotropy, which results in

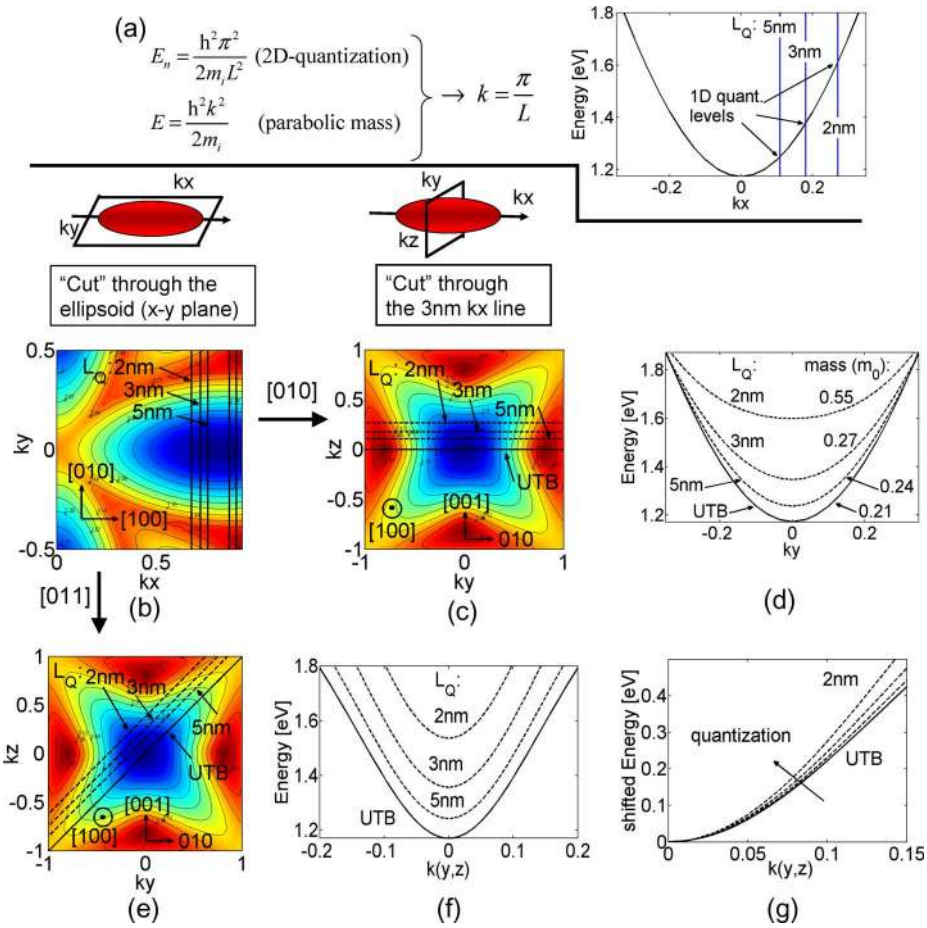


Fig. 7. (a) Energy levels of a quantized structure using the particle-in-a-box picture. Under quantization, the subband edges and masses can be deduced from the materials' bulk dispersion with a numerical $E(k)$ diagram. (b) Energy contour at the middle of one of the Si Brillouin zone ellipsoids calculated using the full 3-D $k$-space information of the Si Brillouin zone. A "cut" through the Si ellipsoid along its longitudinal axis is shown. Under quantization in $Lx = 2$, 3, and 5 nm, respectively, the relevant subband energies are indicated by the vertical $k_x =$ constant lines. (c) A cut through the Si ellipsoid perpendicular to its longitudinal axis at the $k_x$ line corresponding to the 3-nm quantization line of (b). The nonparabolicity and anisotropy is evident in this figure. The horizontal lines indicate the relevant energy regions under another quantization in the $y$-direction for $Ly = 2$-, 3-, and 5-nm quantized structures, respectively. UTB is the relevant band for a UTB device $Lx = 3$ nm thick in [001] with $Lz = \infty$. This is only quantized in the $x$-direction. (d) Dispersions of the vertical lines in (c). The masses and the band edge of the dispersions will be the ones that appear in a quantized wire. (e) The 2-D plot is the same as in (c). The 45° lines correspond to a quantization in [0-11] for $Lyz = 2$, 3, and 5 nm, respectively. UTB is the relevant band for a UTB device $Lx = 3$ nm thick in [001] with $Lyz = \infty$. (f) Dispersions of the 45° lines in (e). Nonparabolicity is evident in this orientation. (g) Zoom of the right (positive momentum) branch of (f) with all dispersions shifted to the origin for comparison. As the structure is quantized in [0-11], the mass becomes lighter. Anisotropy in the Brillouin zone is directly reflected on the masses in the different wire orientations [as in Fig. 6(b)].

different behavior in the quantization of the [100] to quantization of the [110] axes. In [110]-oriented wires, the [100] and [0-11] directions are quantized. The [100] quantization is the same step as the one in Fig. 7(b). Quantizing the [0-11] direction will result in extracting 1-D bands by lines that cross Fig. 7(e) at 45°, (in $Lyz$, instead of horizontal). Fig. 7(f) shows the first subband of the dispersions of structures with $Lx = 3$ nm and $Lyz = 2$ nm, 3nm, 5nm and $\infty$, similar to Fig. 7(d). Evident in this case is the nonparabolicity of the dispersion, also evident in the dispersion of the actual [110] nanowire of Fig. 5(c). For comparison purposes, Fig. 7(g) shows the positive $k_{yz}$ branch of the dispersion, with all the bands shifted to the origin. Clearly, as the structure is quantized in the [0-11] direction, the curvature of the dispersion increases, corresponding to a lowering of the transport mass of the wires. In contrast to the [001] quantization case of Fig. 7(c), here the anisotropy in the bandstructure results in a reduction of the transport masses with increase in quantization, in agreement with the calculation for the actual nanowire mass shown in Fig. 6(b). The magnitude of the mass variation is smaller however, in the [0-11] quantization direction, compared to the [001] direction. (Similar anisotropic results have been also obtained using empirical nonlocal pseudopotential and ab initio GW calculations.[1])

*1) Limitations of the Semi-Analytical Construction:* This construction method can provide a rough guidance as to what the dispersion of a nanowire will look like. This method, however, does not include any of the interactions between the bands/valleys (which are enhanced when the material is physically confined in a nanowire), and lacks any band-coupling information. Effects such as valley splitting, which are a consequence of band coupling, cannot be captured. The extracted mass values, as well as their variation trends under quantization, are quite accurate, however. In the case of nanowire electronic transport for nanowires larger than 3 nm, where the mass is an important transport parameter, a first order estimation of

the nanowires' performance can be drawn using this analytical mass extraction.

## IV. Conclusion

Transport properties of nanowires in different transport orientations ([100], [110], and [111]) are examined using a 10 orbital $sp^3d^5s^*$ atomistic TB model self-consistently coupled to a 2-D Poisson solver. A semiclassical ballistic model was used to calculate the current-voltage characteristics of the nanowires. The dispersions of the nanowires undergo changes under gate bias, which can cause large lift of degeneracies and small subband shifts in some cases. Although these changes under self-consistency do not alter the velocity and density of states of the wires, they are associated with the spatial distribution of charge that, together with the small 1-D density of states, can degrade the nanowire's capacitance by 30%. The quantum capacitance of the different oriented 3-nm wires that are investigated is not only a strong function of gate bias but also of similar magnitude in all wires. Almost the same is also the total gate capacitance of all nanowire devices in the different orientations investigated, as well as the inversion charge. Due to their lighter mass, the 3-nm [110]-oriented wires have the maximum injection velocities, whereas [111]-oriented wires have the lowest injection velocities due to their higher masses. The injection velocity reflects directly on the current capabilities of the wires, where the [110]- and [100]-oriented wires indicate the best performance in terms of ON-current capabilities compared to the [111] wires, which are the worst. The masses of the wires are a sensitive function of the wire dimensions (below 7 nm) and strongly influence the output performance of nanowire devices. This is an effect that resides in the nonparabolicity and anisotropy of the Si Brillouin zone that is particularly important in strongly quantized devices. Valley splitting is another effect strongly dependent on quantization. The [110] nanowires with dimensions below 3 nm are extremely sensitive to this. Finally, the simulator used in this study will be released as an enhanced version of the Bandstructure Lab on nanoHUB.org [34]. This simulation engine allows any user to duplicate the simulation results presented here. Over 800 users have used the Bandstructure Lab in the past 12 months.

## Acknowledgment

The computational resources for this work were provided through nanoHUB.org by the Network for Computational Nanotechnology (NCN). The authors would like to acknowledge Prof. Mark Schilfgaarde of Arizona State University for ab initio GW calculations, Dr. Tony Low of Purdue University for pseudopotential calculations for benchmarking of bandstructure results, and Prof. Timothy Boykin of the University of Alabama at Huntsville for tight-binding discussions.

## References

[1] *ITRS Public Home Page*. [Online]. Available: http://www.itrs.net/reports.html

[2] N. Singh *et al.*, "Ultra-narrow silicon nanowire gate-all-around CMOS devices: Impact of diameter, channel-orientation and low temperature on device performance," in *IEDM Tech. Dig.*, 2006, pp. 1–4.

[3] K. H. Cho, "Observation of single electron tunneling and ballistic transport in twin silicon nanowire MOSFETs (TSNWFETs) fabricated by top-down CMOS process," in *IEDM Tech. Dig.*, 2006, pp. 1–4.

[4] J. Xiang, W. Lu, Y. Hu, Y. Wu, H. Yan, and C. M. Lieber, "Ge/Si nanowire heterostructures as high-performance field-effect transistors," *Nature*, vol. 441, no. 7092, p. 489, May 2006.

[5] T. B. Boykin, G. Klimeck, and F. Oyafuso, "Valence band effective-mass expressions in the $sp^3d^5s^*$ empirical tight-binding model applied to a Si and Ge parametrization," *Phys. Rev. B, Condens. Matter*, vol. 69, no. 11, pp. 115 201–115 210, Mar. 2004.

[6] G. Klimeck, F. Oyafuso, T. B. Boykin, R. C. Bowen, and P. von Allmen, "Development of a nanoelectronic 3-D (NEMO 3-D ) simulator for multimillion atom simulations and its application to alloyed quantum dots," *Comput. Model. Eng. Sci.*, vol. 3, no. 5, pp. 601–642, 2002.

[7] G. Klimeck, S. Ahmed, H. Bae, N. Kharche, S. Clark, B. Haley, S. Lee, M. Naumov, H. Ryu, F. Saied, M. Prada, M. Korkusinski, and T. B. Boykin, "Atomistic simulation of realistically sized nanodevices using NEMO 3-D—Part I: Models and benchmarks," *IEEE Trans. Electron Devices*, vol. 54, no. 9, pp. 2079–2089, Sep. 2007.

[8] J. C. Slater and G. F. Koster, "Simplified LCAO method for the periodic potential problem," *Phys. Rev.*, vol. 94, no. 6, pp. 1498–1524, Jun. 1954.

[9] M. S. Lundstrom and J. Guo, *Nanoscale Transistors: Device Physics, Modeling and Simulation*. New York: Springer-Verlag, 2006.

[10] A. Rahman, J. Guo, S. Datta, and M. Lundstrom, "Theory of ballistic nanotransistors," *IEEE Trans. Electron Devices*, vol. 50, no. 9, pp. 1853–1864, Sep. 2003.

[11] M. Luisier, A. Schenk, and W. Fichtner, "Full-band atomistic study of source-to-drain tunneling in Si nanowire transistors," in *Proc. SISPAD*, 2007, pp. 221–224.

[12] T. B. Boykin, G. Klimeck, M. Friesen, S. N. Coppersmith, P. von Allen, F. Oyafuso, and S. Lee, "Valley splitting in strained silicon quantum wells," *Appl. Phys. Lett.*, vol. 84, no. 1, pp. 115–117, Jan. 2004.

[13] T. B. Boykin, G. Klimeck, M. Friesen, S. N. Coppersmith, P. von Allen, F. Oyafuso, and S. Lee, "Valley splitting in low-density quantum-confined heterostructures studied using tight-binding models," *Phys. Rev. B, Condens. Matter*, vol. 70, no. 16, p. 165 325, Oct. 2004.

[14] A. Rahman, G. Klimeck, M. Lundstrom, T. B. Boykin, and N. Vagidov, "Atomistic approach for nanoscale devices at the scaling limit and beyond—Valley splitting in Si," *Jpn. J. Appl. Phys.*, vol. 44, no. 4B, pp. 2187–2190, 2005.

[15] J. Wang, A. Rahman, A. Ghosh, G. Klimeck, and M. Lundstrom, "On the validity of the parabolic effective-mass approximation for the I–V calculation of silicon nanowire transistors," *IEEE Trans. Electron Devices*, vol. 52, no. 7, pp. 1589–1595, Jul. 2005.

[16] M. Luisier, A. Shenk, W. Fichtner, and G. Klimeck, "Atomistic simulations of nanowires in the $sp^3d^5s^*$ tight-binding formalism: From boundary conditions to strain calculations," *Phys. Rev. B, Condens. Matter*, vol. 74, no. 20, p. 205 323, Nov. 2006.

[17] E. Gnani, S. Reggiani, A. Gnudi, P. Parruccini, R. Colle, M. Rudan, and G. Baccarani, "Band-structure effects in ultrascaled silicon nanowires," *IEEE Trans. Electron Devices*, vol. 54, no. 9, pp. 2243–2254, Sep. 2007.

[18] M. Bescond, N. Cavassilas, and M. Lannoo, "Effective-mass approach for n-type semiconductor nanowire MOSFETs arbitrarily oriented," *Nanotechnology*, vol. 18, no. 25, p. 255 201, Jun. 2007.

[19] Y. Liu, N. Neophytou, T. Low, G. Klimeck, and M. Lundstrom, "A tight-binding study of the ballistic injection velocity for ultrathin-body SOI MOSFETs," *IEEE Trans. Electron Devices*, vol. 55, no. 3, pp. 866–871, Mar. 2008.

[20] N. Neophytou, A. Paul, M. Lundstrom, and G. Klimeck, "Simulations of nanowire transistors: Atomistic vs. effective mass models," *J. Comput. Electron.*, 2008. DOI:10.1007/s10825-008-0188-4.

[21] R. C. Bowen, G. Klimeck, R. Lake, W. R. Frensley, and T. Moise, "Quantitative simulation of a resonant tunneling diode," *J. Appl. Phys.*, vol. 81, no. 7, p. 3207, Apr. 1997.

[22] G. Klimeck, T. B. Boykin, R. C. Bowen, R. Lake, D. Blanks, T. Moise, Y. C. Kao, and W. R. Frensley, "Quantitative simulation of strained and unstrained InP-based resonant tunneling diodes," in *Proc. 55th IEEE Device Res. Conf. Dig.*, 1997, pp. 92–93.

[23] R. C. Bowen, C. Fernando, G. Klimeck, A. Chatterjee, D. Blanks, R. Lake, J. Hu, J. Davis, M. Kularni, S. Hattangady, and I. C. Chen, "Physical oxide thickness extraction and verification using quantum mechanical simulation," in *IEDM Tech. Dig.*, 1997, pp. 869–872.

[24] D. D. D. Ma *et al.*, "Small-diameter silicon nanowire surfaces," *Science*, vol. 299, no. 5614, pp. 1874–1877, Mar. 2003.

[25] J. Wang, "Device physics and simulation of silicon nanowire transistors," Ph.D. dissertation, DAI-B 66/08, p. 4414, Purdue Univ., West Lafayette, IN, Feb. 2006.

[26] X. Zhao, C. M. Wei, L. Yang, and M. Y. Chou, "Quantum confinement and electronic properties of silicon nanowires," *Phys. Rev. Lett.*, vol. 92, no. 23, p. 236 805, Jun. 2004.
[27] N. Kharche, M. Prada, T. B. Boykin, and G. Klimeck, "Valley splitting in strained silicon quantum wells modeled with 2° miscuts, step disorder, and alloy disorder," *Appl. Phys. Lett.*, vol. 90, no. 9, p. 092 109, Feb. 2007.
[28] R. Rahman, C. J. Wellard, F. R. Bradbury, M. Prada, J. H. Cole, G. Klimeck, and L. C. L. Hollenberg, "High precision quantum control of single donor spins in silicon," *Phys. Rev. Lett.*, vol. 99, no. 3, p. 036 403, Jul. 2007.
[29] G. Liang, J. Xiang, N. Kharche, G. Klimeck, C. M. Lieber, and M. Lundstrom, "Performance analysis of a Ge/Si core/shell nanowire field-effect transistor," *Nano Lett.*, vol. 7, no. 3, pp. 642–646, 2007.
[30] S. Lee, F. Oyafuso, P. Von, and G. Allmen, "Boundary conditions for the electronic structure of finite-extent embedded semiconductor nanostructures," *Phys. Rev. B, Condens. Matter*, vol. 69, no. 4, pp. 045 316–045 323, Jan. 2004.
[31] N. Neophytou, A. Paul, M. Lundstrom, and G. Klimeck, "Self-consistent simulations of nanowire transistors using atomistic basis sets," in *Proc. SISPAD*, 2007, pp. 217–220.
[32] H. S. Pal, K. D. Cantley, S. S. Ahmed, and M. S. Lundstrom, "Influence of bandstructure and channel structure on the inversion layer capacitance of Si and GaAs MOSFETs," *IEEE Trans. Electron Devices*, vol. 55, no. 3, 2008.
[33] A. Rahman, M. S. Lundstrom, and A. W. Ghosh, "Generalized effective-mass approach for n-type metal-oxide-semiconductor field-effect transistors on arbitrarily oriented wafers," *J. Appl. Phys.*, vol. 97, no. 5, pp. 053 702–053 713, Mar. 2005.
[34] *[nanoHub] Bandstructure lab on nanoHUB.org*. [Online]. Available: https://www.nanohub.org/tools/bandstrlab/

**Neophytos Neophytou** received the B.S. degree in electrical and computer engineering in 2001 and the M.S. degree in 2003 in microelectronics and nanotechnology, both from Purdue University, West Lafayette, IN. He is currently pursuing the Ph.D. degree at Purdue University.

His research interests include computational modeling of quantum–mechanical electron transport through new channel materials such as carbon nanotubes, nanowires, grapheme-based channels, and III–V materials. He is currently working on the effects of bandstructures on the electronic properties of nanoscale devices, as well as the effect of atomistic variations and defects in their transport capabilities.

**Abhijeet Paul** received the B.S. degree in electrical engineering from Indian Institute of Technology, (IIT) Bombay, India, and the M.S. degree in microelectronics also from IIT Bombay in 2006, during which he developed a simulator to estimate and predict the threshold voltage shifts in SONOS Flash memories. He is presently pursuing the Ph.D. degree in the field of nanoelectronics in electrical engineering at Purdue University, West Lafayette, IN.

His research interests involve modeling quantum transport in nanosized devices and understanding their electronic properties. He is also involved in tool development, a topic found on http://nanoHUB.org.

**Mark S. Lundstrom** received the B.E.E. and M.S.E.E. degrees from the University of Minnesota, Minneapolis, in 1973 and 1974, respectively. He received the Ph.D. degree in electrical engineering from Purdue University, West Lafayette, IN in 1980.

From 1974 to 1977, he worked at Hewlett-Packard Corporation, Loveland, CO, on integrated circuit process development and manufacturing support. In 1980, he joined the School of Electrical Engineering, Purdue University where he is currently the Don and Carol Scifres Distinguished Professor of Electrical and Computer Engineering and the founding director of the Network for Computational Nanotechnology. From 1989 to 1993 he was a director of Purdue University's Optoelectronics Research Center, and from 1991 to 1994 he was Assistant Dean of Engineering. His current research interests center on the physics of small electronic devices, especially nanoscale transistors, and on carrier transport in semiconductor devices.

Dr. Lundstrom is a Fellow of the American Physical Society and of the American Association for the Advancement of Science. In 1992, he received the Frederick Emmons Terman Award from the American Society for Engineering Education. In 2005, he received the Semiconductor Industry Association's University Researcher Award for his career contributions to the physics and simulation of semiconductor devices. He is currently a Distinguished Lecturer at the IEEE Electron Devices Society. With his colleague, S. Datta, Lundstrom was awarded the 2002 IEEE Cledo Brunetti award for their work on nanoscale electronic devices. They shared the Semiconductor Research Corporation's Technical Excellence Award that same year. Most recently, he received the IEEE Electron Devices Society's Education Award in 2006.

**Gerhard Klimeck** received the German electrical engineering degree from Ruhr-University Bochum, in 1990, and the Ph.D. degree from Purdue University, West Lafayette, IN, in 1994.

He is the Associate Director for Technology of the Network for Computational Nanotechnology and Professor of Electrical and Computer Engineering at Purdue University. He leads the development and deployment of Web-based simulation tools that are hosted on http://nanoHUB.org a community website that was used by over 58 000 users in the year 2007. He was the Technical Group Supervisor for the Applied Cluster Computing Technologies Group and continues to hold his appointment as a Principal Member at the NASA Jet Propulsion Laboratory, Pasadena, CA, on a faculty part-time basis. Previously, he was a member of the technical staff at the Central Research Lab of Texas Instruments, Dallas. His research interest is in the modeling of nanoelectronic devices, parallel cluster computing, and genetic algorithms. He has the led the development of NEMO 3-D, a tool that enables the simulation of tens-of-million atom quantum dot systems, and NEMO 1-D, the first nanoelectronic CAD tool. His work is documented in over 180 peer-reviewed publications and over 310 conference presentations.

Dr. Klimeck is a member of the American Physical Society, Eta Kappa Nu, and Tau Beta Pi. More information can be found at http://www.ece.purdue.edu/~gekco and http://nanoHUB.org/klimeck.